NIR-II fluorescence-guided liver cancer surgery by a small molecular HDAC6 targeting probe

Bo Wang,[a,b,h] Chu Tang,[e,h] En Lin,[a,b,h] Xiaohua Jia,[b,c,h] Ganyuan Xie,[a] Peiping Li,[a] Decheng Li,[a] Qiyue Yang,[f] Xiaoyong Guo,[b,g] Caiguang Cao,[b,c] Xiaojing Shi,[b,c] Baojia Zou,[a] Chaonong Cai,[a] Jie Tian,[b,c,d,e,h,*] Zhenhua Hu,[b,c,h,**] and Jian Li[a,h,***]

[a]Department of Hepatobiliary Surgery and Liver Transplantation, The Fifth Affiliated Hospital of Sun Yat-sen University, Zhuhai, 519000, China
[b]CAS Key Laboratory of Molecular Imaging, Beijing Key Laboratory of Molecular Imaging, Institute of Automation, Chinese Academy of Sciences, Beijing, 100190, China
[c]School of Artificial Intelligence, University of Chinese Academy of Sciences, Beijing, 100049, China
[d]Beijing Advanced Innovation Center for Big Data-Based Precision Medicine, School of Engineering Medicine, Beihang University, Beijing, 100191, China
[e]Engineering Research Center of Molecular and Neuro Imaging of Ministry of Education, School of Life Science and Technology, Xidian University, Xi'an, 710071, China
[f]Key Laboratory of Digital Hepatobiliary Surgery, PLA, Institute of Hepatobiliary Surgery of Chinese PLA, Beijing, 100048, China
[g]Clinical College of Armed Police General Hospital of Anhui Medical University, Department of Gastroenterology of The Third Medical Center of Chinese PLA General Hospital, Beijing, 100039, China

eBioMedicine
2023;98: 104880
Published Online xxx
https://doi.org/10.1016/j.ebiom.2023.104880

Summary

Background Hepatocellular carcinoma (HCC) is the sixth most common malignancy globally and ranks third in terms of both mortality and incidence rates. Surgical resection holds potential as a curative approach for HCC. However, the residual disease contributes to a high 5-year recurrence rate of 70%. Due to their excellent specificity and optical properties, fluorescence-targeted probes are deemed effective auxiliary tools for addressing residual lesions, enabling precise surgical diagnosis and treatment. Research indicates histone deacetylase 6 (HDAC6) overexpression in HCC cells, making it a potential imaging biomarker. This study designed a targeted small-molecule fluorescent probe, $SeCF_3$-IRDye800cw ($SeCF_3$-IRD800), operating within the Second near-infrared window (NIR-II, 1000–1700 nm). The study confirms the biocompatibility of $SeCF_3$-IRD800 and proceeds to demonstrate its applications in imaging *in vivo*, fluorescence-guided surgery (FGS) for liver cancer, liver fibrosis imaging, and clinical samples incubation, thereby preliminarily validating its utility in liver cancer.

Methods $SeCF_3$-IRD800 was synthesized by combining the near-infrared fluorescent dye IRDye800cw-NHS with an improved HDAC6 inhibitor. Initially, a HepG2-Luc subcutaneous tumor model (n = 12) was constructed to investigate the metabolic differences between $SeCF_3$-IRD800 and ICG *in vivo*. Subsequently, HepG2-Luc (n = 12) and HCCLM3-Luc (n = 6) subcutaneous xenograft mouse models were used to assess *in vivo* targeting by $SeCF_3$-IRD800. The HepG2-Luc orthotopic liver cancer model (n = 6) was employed to showcase the application of $SeCF_3$-IRD800 in FGS. Liver fibrosis (n = 6) and HepG2-Luc orthotopic (n = 6) model imaging results were used to evaluate the impact of different pathological backgrounds on $SeCF_3$-IRD800 imaging. Three groups of fresh HCC and normal liver samples from patients with liver cancer were utilized for $SeCF_3$-IRD800 incubation *ex vivo*, while preclinical experiments illustrated its potential for clinical application.

Findings The HDAC6 inhibitor 6 ($SeCF_3$) modified with trifluoromethyl was labeled with IRDy800CW-NHS to synthesize the small-molecule targeted probe $SeCF_3$-IRD800, with NIR-II fluorescence signals. $SeCF_3$-IRD800 was rapidly metabolized by the kidneys and exhibited excellent biocompatibility. *In vivo* validation demonstrated that $SeCF_3$-IRD800 achieved optimal imaging within 8 h, displaying high tumor fluorescence intensity (7658.41 ± 933.34) and high tumor-to-background ratio (5.20 ± 1.04). Imaging experiments with various expression levels revealed its capacity for HDAC6-specific targeting across multiple HCC tumor models, suitable for NIR-II intraoperative imaging. Fluorescence-guided surgery experiments were found feasible and capable of

*Corresponding author. CAS Key Laboratory of Molecular Imaging, Beijing Key Laboratory of Molecular Imaging, Institute of Automation, Chinese Academy of Sciences, Beijing, 100190, China.
**Corresponding author. CAS Key Laboratory of Molecular Imaging, Beijing Key Laboratory of Molecular Imaging, Institute of Automation, Chinese Academy of Sciences, Beijing, 100190, China.
***Corresponding author.
E-mail addresses: jie.tian@ia.ac.cn (J. Tian), zhenhua.hu@ia.ac.cn (Z. Hu), lijian5@mail.sysu.edu.cn (J. Li).
[h]These authors contributed equally.

detecting sub-visible 2 mm tumor lesions under white light, aiding surgical decision-making. Further imaging of liver fibrosis mice showed that $SeCF_3$-IRD800's imaging efficacy remained unaffected by liver pathological conditions. Correlations were observed between HDAC6 expression levels and corresponding fluorescence intensity (R^2 = 0.8124) among normal liver, liver fibrosis, and HCC tissues. $SeCF_3$-IRD800 identified HDAC6-positive samples from patients with HCC, holding advantages for perspective intraoperative identification in liver cancer. Thus, the rapidly metabolized HDAC6-targeted small-molecule NIR-II fluorescence probe $SeCF_3$-IRD800 holds significant clinical translational value.

Interpretation The successful application of NIR-II fluorescence-guided surgery in liver cancer indicates that $SeCF_3$-IRD800 has great potential to improve the clinical diagnosis and treatment of liver cancer, and could be used as an auxiliary tool for surgical treatment of liver cancer without being affected by liver pathology.

Funding This paper is supported by the National Natural Science Foundation of China (NSFC) (92,059,207, 62,027,901, 81,930,053, 81,227,901, 82,272,105, U21A20386 and 81,971,773), CAS Youth Interdisciplinary Team (JCTD-2021-08), the Zhuhai High-level Health Personnel Team Project (Zhuhai HLHPTP201703), and Guangdong Basic and Applied Basic Research Foundation under Grant No. 2022A1515011244.

Keywords: Hepatocellular carcinoma; Second near-infrared window; Molecular imaging; HDAC6; Fluorescence-guided surgery

Research in context

Evidence before this study

The residual lesion of hepatocellular carcinoma (HCC) is a major challenge for surgeons. Fluorescence imaging technology can help doctors to make decisions to achieve accurate tumor resection. For decades, fluorescence imaging has been proven to be able to visualize tumors at molecular and cell levels, assisting doctors in intraoperative diagnosis and treatments. We conducted a systematic search of several databases, including PubMed, Embase, and Medicine, from the date of creation to November 30, 2022, for categories such as "Hepatocellular carcinoma", "Near-infrared fluorescence" and "Fluorescent-guided surgery". However, most relevant research focuses on the first near-infrared window (NIR-I, 700–900 nm). In recent years, NIR-II fluorescence imaging has advantages in tissue penetration depth, imaging resolution, and lower spontaneous fluorescence than NIR-I. There are few studies on the application of NIR-II in the imaging of liver cancer.

Added value of this study

In this study, $SeCF_3$-IRD800 targeting HDAC6 was synthesized to realize the labeling of HDAC6-positive tumor cells *in vivo*. Imaging experiments were carried out in various tumor models and disease models, and the targeting and clinical transformation potential of $SeCF_3$-IRD800 was verified in fresh liver and cancer tissue specimens. The expression levels of HDAC6 in both cancerous tissues and the liver were comprehensively analyzed.

Implications of all the available evidence

This study broke through the dilemma of high background fluorescence signal and poor liver imaging effect caused by non-specific aggregation. It provides a new technique for the treatment of HCC. It not only enables *in-situ* imaging and fluorescent-guided resection, but the imaging efficiency is independent of the pathology of the liver itself which can help surgeons remove lesions precisely and has great clinical translation potential.

Introduction

Hepatocellular carcinoma (HCC) is the sixth most common malignancy and the third most common cause of cancer death worldwide.[1] About 70% of patients with liver cancer have an advanced stage at the initial diagnosis. Although hepatectomy is the main treatment method and potential means,[2] the 5-year survival rate of the middle and advanced stages is only 6.5%.[3]

At present, the preoperative diagnosis of HCC relies on imaging detection, such as ultrasound (US), computed tomography (CT), and magnetic resonance imaging (MRI), but the diagnostic efficacy for small lesions less than 2 cm is limited.[4,5] Surgeons distinguish benign and malignant tissues mainly through the visual examination and palpation during surgery,[6] due to the variable situation of the operation and the different professional abilities of surgeons, there are limitations in the identification of small lesions and surgical margins. Up to 70% of the 5-year postoperative recurrence rate was reported in patients with liver cancer.

In the past decade, the interdisciplinary research in medical engineering driven by molecular imaging

technology and artificial intelligence has brought great progress to the development of basic medicine and the improvement of clinical skills.[7–13] Since 2009, when Indocyanine green (ICG) was first employed in fluorescence-guided surgery (FGS),[14–16] fluorescence imaging technology has achieved multi-dimensional clinical applications in open surgery and laparoscopic surgery.[17] FGS has been proven to be a safe technique, that can assist surgeons in intraoperative decision-making and achieve accurate visual tumor resection, such as surgical margin determination and microscopic lesion detection.[18] ICG is the most commonly used non-targeted near-infrared dye approved by the FDA,[19] which has been widely used in FGS in various disciplines such as the digestive tract[20,21] and gynecological surgery.[22] It is of great importance in the differentiation degree of primary liver cancer,[22] identification of liver segments,[23,24] determination of intraoperative focal boundaries of cancer,[18] detection of micro-lesions, exploration of metastatic cancer, biliary tract imaging,[25] liver transplantation[26,27] and so on. However, ICG can accumulate in non-cancer tissues in a non-specific way, leading to a higher false positive rate.[19,28] Currently, a series of clinical trials of targeted ligands based on ICG or IRDye800cw labeling has been used for targeted fluorescence imaging to achieve rapid and accurate imaging of patients with intraoperative residual tumors and lymph nodes.[29,30] At present, most FGS studies are in the first near-infrared window (NIR-I, 700–900 nm).[19] With the development of fluorescence imaging technology in the second near-infrared window (NIR-II, 1000–1700 nm), its imaging quality is much better than that of traditional NIR-I fluorescence imaging due to high imaging resolution, low background, spontaneous fluorescence, deep tissue imaging capability, etc.[31] Currently, a phosphorescent probe[32–34] and radiopharmaceutical-excited nanoparticles[35] have been developed for the imaging of NIR-II. NIR-II imaging has also been widely used in the imaging of cirrhotic liver cancer,[36] high-grade glioma,[11] cystic renal masses,[37] gray fat, and bone.[38] Previous studies of FGS for HCC by ICG have shown that NIR-II imaging has a higher sensitivity in the detection of minor tumors, compared with NIR-I imaging.[31] Therefore, it is urgent to prepare a sensitive and specific HCC small molecule targeted fluorescent probe to achieve FGS in HCC resection.

Histone deacetylases (HDACs) catalyze the deacetylation of lysine residues of histones and non-histones.[39] To date, much evidence suggests that HDACs play an important role in the process of cancer proliferation and spread, and unusually high levels of HDACs have been found in various cancers. For example, the high expression of HDAC6 can promote the proliferation of tumor cells,[40,41] accelerate the early invasion and metastasis of HCC, and promote tumor angiogenesis,[42] which is a potential target for tumor research. Although it has been reported that HDAC6 can act as a tumor suppressor to inhibit the development and progression of HCC. However, it has also been shown that HDAC6 can participate in tumor promotion by inhibiting the transcriptional activity of p53 or accelerating the migration and invasion of HCC cells in HCC.[41,43,44] Currently, various HDAC6 inhibitors have been designed and developed for the treatment of a variety of cancers, but few probes have been developed for HDAC6 imaging.[45–48] Therefore, the development of HDAC6-targeted near-infrared fluorescent probes may be a promising auxiliary tool for fluorescence navigation surgery of HCC.

A trifluoromethyl-modified HDAC6 inhibitor, 6($SeCF_3$), was labeled as a targeting probe IRDye800cw-$SeCF_3$ ($SeCF_3$-IRD800) by IRDye800cw-NHS with NIR-II window fluorescence signal. In this study, the biosafety of the probe was evaluated. In terms of imaging, the probe was used for NIR-II FGS for liver cancer and *in vivo* imaging of liver fibrosis, respectively. We further verified the expression of HDAC6 in pairs of samples from patients with liver cancer, and samples from patients with liver cancer were used to be incubated by the probe. The data suggest that the NIR-II fluorescent small-molecule targeting probe, $SeCF_3$-IRD800, has excellent imaging and metabolic characteristics. In brief, $SeCF_3$-IRD800 is of tremendous clinical transformation value.

Methods

Ethics statement

Written informed consent was obtained from each subject according to the Declaration of Helsinki, and the study was approved by the Ethics Committee of the Fifth Affiliated Hospital of Sun Yat-Sen University (ethics number: L002-1). All animal experiments were conducted under the supervision of the Experimental Animal Ethics Committee of the Institute of Automation, Chinese Academy of Sciences (ethic number: IA21-2203-13).

Western blot

Normal liver cell line HL-7702 (LO_2) (KCB Cat# KCB 200511 YJ, RRID: CVCL_6926), HCC HepG2-luc (RRID: CVCL_JG47), Huh7 (RRID: CVCL_0336), PLC/PRF/5 (RRID: CVCL_0485), HCCLM3 (RRID: CVCL_6832), and Bel-7402 (RRID: CVCL_5492) cell lines were purchased from Beijing Beina Biotechnology Co., LTD. Primary HCC cell was derived from a patient with HCC. All cells were cultured with Dulbecco's minimum essential medium (DMEM, M&C GENE Technology (Beijing) Ltd.) containing 10% fetal bovine serum (FBS, M&C GENE Technology (Beijing) Ltd.) and 1% penicillin-streptomycin. All cell lines were maintained in a 5% CO_2 incubator at 37 °C. All cells have been authenticated for purity and identity through short tandem repeat (STR) profiling.

Western blot was used to analyze HDAC6 expression levels at the cellular level. RIPA buffer containing protease and protein phosphatase inhibitor is used to lysate cells, BCA protein (G5001, Servicebio, Wuhan, China) test kit is used to determine protein concentration. The protein samples were then boiled for 10 min, and the total protein of 20 μg was electrophoresed on 10% SDS-polyacrylamide gel and transferred to the PVDF membrane. The membrane was blocked with 5% bovine serum albumin at room temperature (RT) for 2 h. A 1:500 diluted anti-HDAC6 antibody (Abcam Cat# ab53099, RRID: AB_880359) was stored in the refrigerator at 4 °C overnight and GAPDH (Abcam Cat# ab9485, RRID: AB_307275) was used as an endogenous control. The samples were washed 3 times in TBST, and incubated with HRP-conjugated goat anti-rabbit secondary antibody (ServiceBio Cat# GB23303, RRID: AB_2811189) for about 1 h at RT. Finally, HDAC6 expression was detected by enhanced chemiluminescence, imaged using the Alliance MINI HD 6 analyzer (UVITEC, UK), and calculated by quantitative western blot strip strength using ImageJ.

Synthesis of tert-butyl (4-(6-((trifluoromethyl) selanyl) hexanamido) phenyl) carbamate (2)

As shown in Fig. S1, a solution of compound **1** (410 mg, 1.0 mmol) in THF (30 mL) was added to TBAF (262 mg, 2.0 mmol) and $TMSCF_3$ (1.137 mg, 8.0 mmol). The reaction solution was stirred at room temperature for 2 h. The solvent was removed under reduced pressure to yield crude product, which was purified by silica gel column chromatography (Petroleum ether-EtOAc, 6:4). Yield: 71%. White solid.

Synthesis of *N*-(4-aminophenyl)-6-((trifluoromethyl)selanyl) hexanamide

Next, trifluoroacetic acid (TFA, 1 mL) was added slowly to a solution of compound **2** (227 mg, 0.5 mmol) in CH_2Cl_2 (20 mL) at 0 °C. Then, the reaction solution was stirred at 0 °C for 3 h, diluted with water (20 mL), and extracted with ethyl acetate (3 × 20 mL). The extracts were dried with Na_2SO_4 and evaporated in vacuo. The crude product was purified by silica gel column chromatography (methylene chloride-methanol, 8:1) to give **3**. Yield: 91%. White solid. ^1H NMR (400 Hz, CD_3OD) δ 7.23 (d, J = 7.2 Hz, 2H), 6.68 (d, J = 7.2 Hz, 2H), 3.05 (t, J = 4.8 Hz, 2H), 2.33 (t, J = 5.2 Hz, 2H), 1.81–1.86 (m, 2H), 1.67–1.72 (m, 2H), 1.46–1.51 (m, 2H).

Synthesis of $SeCF_3$-IRD800

Finally, to a solution of IRDye800cw-NHS (1.0 mg, 0.96 μmol) in DMSO (2 mL), compound **3** (0.5 mg, 1.5 μmol) and Et_3N (20 μL) were added and stirred in the dark at room temperature for 24 h. Then, the crude product was purified by HPLC on a C-18 column (20 mm × 250 mm) using gradient elution with CH_3CN (0.1% TFA) and H_2O as solvents A and B, respectively. The flow rate was 12 mL/min. The fractions containing $SeCF_3$-IRD800 were collected and lyophilized. The purified $SeCF_3$-IRD800 was obtained as a green solid with 84% yield and over 98% purity. MS (ESI): m/z 1360.4 ($[M + Na]^+$).

$SeCF_3$-IRD800 characterization

The excitation spectra and absorption spectra were determined on a Shimadzu UV-2600 UV–Vis spectrophotometer, and the emission spectra were measured on FLS980 (Edinburgh Instruments). NIR-II fluorescence imaging was implemented with an InGaAs SWIR camera (Xenics Cheetah-640CL TE3) coordinated with a lens (Spacecom VF50M SWIR) that can transmit NIR-II light, and a filter wheel (1000 nm, 1100 nm, 1200 nm, 1300 nm, 1400 nm, 1500 nm, Thorlabs, USA) was fixed in the front end of the lens to capture NIR-II fluorescence. The NIR-II imaging field of view was approximately 10 cm. The wavelength of the excitation laser was 808 nm with the power set to be 21.10 mW/cm^2, and the exposure time was 0.3–2.0 s. All signals were detected utilizing a 1000 nmLP filter unless otherwise specified. To explore the relationship between the fluorescence intensity of $SeCF_3$-IRD800 and concentration, a multiple dilution method was used to set the concentration gradients of 0,12.5, 25, 50, 75, 100, 150, or 200 μg/mL $SeCF_3$-IRD800 solution with PBS as the solvent. The influence of different solvents on $SeCF_3$-IRD800 imaging efficiency was further studied. Fetal bovine serum (FBS) and PBS were used as solvents, and the same concentration gradient was set as above. Each concentration was set for three repetitions. The experimental procedure involved using 6-week-old male Balb/c nude mice for vessel imaging. $SeCF_3$-IRD800 (0.3 mg/mL) was administered intravenously via the tail vein. Fluorescence images were captured at wavelengths of 1000 nm, 1100 nm, 1200 nm, 1300 nm, and 1400 nm using the aforementioned NIR-II equipment. The excitation laser utilized was 808 nm with an exposure time ranging from 10 ms to 1 s. A Complementary Metal Oxide Semiconductor (CMOS) camera (PCO. edge 5.5, PCO, Germany) equipped with an 850 ± 40 nm bandpass filter was employed to acquire NIR-I fluorescence images. The excitation laser used for NIR-I imaging was 792 nm, while the exposure time was set to 30 ms. All images were collected at RT. ImageJ software (National Institutes of Health, USA, http://imagej.nih.gov/ij) was used to analyze the data.

In vitro and in vivo toxicity of *$SeCF_3$-IRD800*

For cell proliferation inhibition assays, 1×10^5 cells were inoculated into each well of a 96-well plate and cultured at 37 °C in a 5% CO_2 incubator for 24 h. After the cells were stimulated for 24 h by adding 0, 4.375, 8.75, 17.5, 35, 70, 140, or 280 μg/mL of $SeCF_3$-IRD800, the cell supernatant was discarded, and fresh complete medium

was added. Then, 10 μl of CCK-8 solution was added and cultured for 3 h. The absorbance was measured at 450 nm with a microplate reader.

Male Balb/c nude mice (6 weeks old) were purchased from Beijing Vital River Laboratory Animal Technology Co., Ltd (Beijing, Chaoyang). The $SeCF_3$-IRD800 (200 nmol) in 100 μL PBS (M&C GENE Technology (Beijing) Ltd.) was injected into healthy mice. The blood samples were collected at 3 days (n = 3) and 30 days (n = 3) after injection (500 μl per mouse), and after being placed at RT for 1 h, the upper serum was centrifuged by ultra-fast refrigerated centrifuge (4 °C, 15,000 rpm). Liver function (AST, ALT, ALB) and renal function (BUN, CREA, UA) were monitored. Then, the mice were sacrificed and major organs were dissected and stained with hematoxylin and eosin (HE staining) for histology analysis.

Construction of mouse liver cancer Xenograft Models or hepatic fibrosis models

All mice were purchased from Beijing Vital River Laboratory Animal Technology Co.Ltd. (Beijing, Chaoyang) and were raised under standard conditions in the Zoology Hall of the Institute of Automation, Chinese Academy of Sciences. High and low HDAC6 expression level HCC cell lines HepG2 labeled luciferase (HepG2-luc) and HCCLM3-luc were used to construct the subcutaneous tumor and *in situ* liver tumor models of male Balb/c nude mice aged 4 weeks, respectively. Then, 2×10^6 cells were mixed with 100 μl PBS and implanted subcutaneously. The mice were kept warm after the operation. Tumor growth was observed two weeks later. Similarly, 2×10^6 cells were mixed with the same volume of PBS and Matrigel basement membrane matrix (Biocota, Corning) and implanted under the liver capsule. Post-anesthesia air embolism in mice with excessive tumor burden or age.

Balb/c mice, male, 4 weeks, were selected to establish hepatic fibrosis models. Induction methods were performed by intraperitoneal injection of CCl_4 solution (60% olive oil, 2 mL/kg, twice a week for 6 weeks). Then Sirius scarlet staining was used to demonstrate the degree of fibrosis after NIR-II imaging. Immunohistochemistry (IHC) was used to evaluate HDAC6 expression in hepatic fibrosis tissues.

Bioluminescence imaging

The IVIS Spectral *in vivo* Imaging System (Caliper Life Sciences, Waltham, Massachusetts) is being used to acquire bioluminescent imaging (BLI) to locate tumors. The tumor-bearing mice were anesthetized with 2% isoflurane and intraperitoneal injected with 150 mg/kg/100 μL of normal saline. BLI images were collected 5 min after injection of D-luciferin. IVIS CT-BLI fusion scanning was used for *in vivo* three-dimensional (3D) reconstruction of tumors.

NIR-II fluorescence imaging

Tumor-bearing mice (n = 12) were randomly divided into two groups, one of which was injected with $SeCF_3$-IRD800 (150 μg/mL, 120 μl), and the other group was injected with ICG solution (0.25 mg/kg, 120 μl). NIR-II images were collected before injection (0 h), 2, 4, 6, 8, 10, 12, 24, and 48 h after injection, and the fluorescence intensity of the tumor area, Tumor to background signal ratio (TBR), and the fluorescence signal of the liver area on the body surface were counted. All images were collected with the exposure time 0.3 s∼1 s.

Tumor-bearing mice (n = 4) were sacrificed 8 h after $SeCF_3$-IRD800 injection and their major organs, tumors, and gastric contents were isolated for *ex-vivo* NIR-II imaging. The fluorescence intensity of each sample was measured, and the fluorescence signal ratios of tumors and major organs to the liver were calculated.

The mice with liver fibrosis (n = 6) and orthotopic liver cancer (n = 6) were injected with the same dose of $SeCF_3$-IRD800. NIR-II imaging was performed 8 h after *in vivo* liver exposure to measure the fluorescence signal intensity of the fibrotic liver, normal liver, and tumor areas. These mice were then sacrificed, and HE and IHC staining were used to evaluate HDAC6 expression, while Sirius red staining was used to determine the degree of fibrosis.

In vivo targeting evaluation

A total of eighteen mice with subcutaneous tumors were divided into three groups: high HDAC6 expression imaging group (Imaging/HepG2, n = 6), low HDAC6 expression imaging group (Imaging/HCCLM3, n = 6), and blocking group (Blocking/HepG2, n = 6). The Blocking/HepG2 group received a slow injection of a 1.8 mg/mL aqueous solution of Vorinostat (SAHA) (Beijing InnoChem Science & Technology Co. Ltd.) (IC50 = 2.7 mg/mL) at a volume of 500 μl, which was 55-fold greater in concentration than the $SeCF_3$-IRD800 concentration. The other two groups were injected with 500 μl of PBS. After 45 min of SAHA or PBS injection, all mice were injected with 150 μg/mL and 120 μl $SeCF_3$-IRD800. NIR-II fluorescence images were obtained at 0, 4, 8, 12, and 24 h after injection, and subsequently analyzed using ImageJ software. IHC was performed to confirm the HDAC6 expression level in the tumors. The mice were kept warm throughout the experimental duration.

NIR-II fluorescence image-guided surgery on tumor-bearing mice

The IVIS CT-BLI fusion scan was used for preoperative three-dimensional tumor reconstruction in mice with HepG2-Luc tumors. The mice were injected with $SeCF_3$-IRD800 (150 μg/mL, 120 μl) intravenously 8 h before surgery. Before tumor resection, the mice were anesthetized and positioned on the operating table. The surgical approach involved visual diagnosis and NIR-II

fluorescence exploration. The visible tumor was first removed through visual inspection, followed by NIR-II imaging in the surgical area to confirm the absence of any remaining lesions based on visual or fluorescence examination. The presence of tumor tissue was confirmed using HE staining.[49]

HE staining and immunohistochemistry

Tumors and major organs dissected from mice models were fixed in 4% paraformaldehyde. The fixed tissues were then embedded in paraffin. Sections (4-μm thick) were cut and stained with HE staining.

A total of 29 pairs of HCC samples with their corresponding noncancerous liver tissues from patients with HCC and 4 additional cases of fatty liver tissues were obtained from the Department of Hepatobiliary Surgery and Liver Transplantation, the Fifth Affiliated Hospital of Sun Yat-Sen University. All tissues came from patients with liver cancer who underwent surgical treatment in the above department between June 2018 and August 2020. All information about the participants was obtained from recorded patient reports, and information about tumor size, major or micro-vascular invasion, metastasis, postoperative recurrence, postoperative pathology reports, and postoperative follow-up were obtained from medical records from patients. Sex information was obtained through self-reporting by research participants. Fresh samples derived from patients with HCC for IHC were provided by the Department of Hepatobiliary Surgery, Chinese PLA General Hospital. Immunohistochemistry was applied to all clinical samples to analyze HDAC6 expression. A rabbit polyclonal anti-HDAC6 antibody (Beijing Zhongyuan Heju Biotechnology Co., LTD) (Abcam Cat# ab61173, RRID: AB_941881), HRP-conjugated goat anti-rabbit secondary antibody (Service-bio, Wuhan, China) (ServiceBio Cat# GB23303, RRID: AB_2811189) were used for IHC, respectively.

Incubation and *Ex vivo* imaging of fresh samples derived from patients with HCC

Tumor and liver tissues were collected during surgery and immediately placed in PBS. The specimens were shaken at 60 rpm for 5 min, repeated 3 times. One tumor tissue was incubated with SAHA at a concentration of 100 μM/mL for 45 min, followed by incubation in $SeCF_3$-IRD800 at a concentration of 20 μM/mL. After 45 min of incubation, the PBS washing procedure described above was repeated.[50] Fluorescence imaging of the above specimens was performed by the above NIR-II imaging system with a 300 ms exposure time and 1000 nmLP filter. The excitation wavelength was 808 nm and fluorescence above 1000 nm was collected.[51] The samples were then fixed in 4% formaldehyde and embedded in paraffin. Three consecutive sections with a thickness of 4 μm were cut from the embedded tissues. HE staining and immunohistochemical staining were performed on these sections.

Statistical analysis

The experimental data were analyzed using GraphPad Prism 9.5 and presented as mean ± standard deviation (SD). Student's t-test for comparing two groups, simple linear regression for assessing the correlation between two quantitative variables, Multiple comparison for analyzing differences between multiple variables, and Chi-square test for analyzing contingency tables. When $*p < 0.05$, it was statistically significant (*, **, ***, and **** represents $p < 0.05$, $p < 0.01$, $p < 0.001$ and $p < 0.0001$). ImageJ was used to quantify data and convert it into pseudo color. Image-Pro Plus 6.0 was employed to analyze the expression of HDAC6 in IHC.

Role of the funding source

The sponsors of the study had no role in the study design, data collection, data analyses, data interpretation, manuscript writing, or the decision to submit the paper for publication.

Results

Expression of HDAC6 in cell lines and samples from patients with HCC

Western blot was used to detect the expression of HDAC6 in human normal liver cells LO2, HCCLM3, PLC/PRF-5, HepG2, Huh7, Bel-7402 liver cancer cells, and primary liver cancer cells. HDAC6 is the highest expressed in HepG2, and HCCLM3 had low expression (Fig. 1a). Bands quantitative analysis showed that the gray value ratio of HDAC6 and internal reference GAPDH in primary HCC cell, LO2, HepG2, and HCCLM3 was 0.93, 0.02, 1.30, and 0.65, respectively (Fig. 1b). These results provided a basis for the establishment of tumor-bearing mice models. HDAC6 expression in HCC tissues was significantly higher than in peritumoral normal tissues among the 29 pairs of samples from patients with liver cancer (****$p < 0.0001$, Multiple comparison) (Fig. 1c). Out of the 29 patients, 23 showed higher HDAC6 expression in cancer tissue compared to normal tissue, resulting in a positive classification. Thus, the positive rate of HDAC6 in patients with HCC was 79.3%. Among the patients with recurrence, 80.0% (12/15) exhibited a positive rate of HDAC6. However, analyzing the baseline characteristics of patients revealed no heightened recurrence risk for those with a high HDAC6 expression (Chi-square test) (Table S1). This discrepancy may be attributed to the significant heterogeneity among patients with HCC or the limited sample size. To address this, we classified the clinical samples into various pathological types, including HCC (n = 29), normal liver (n = 17), fatty liver (4 additional fatty liver tissues were included, n = 5), and liver fibrosis (n = 11), and conducted an IHC analysis to

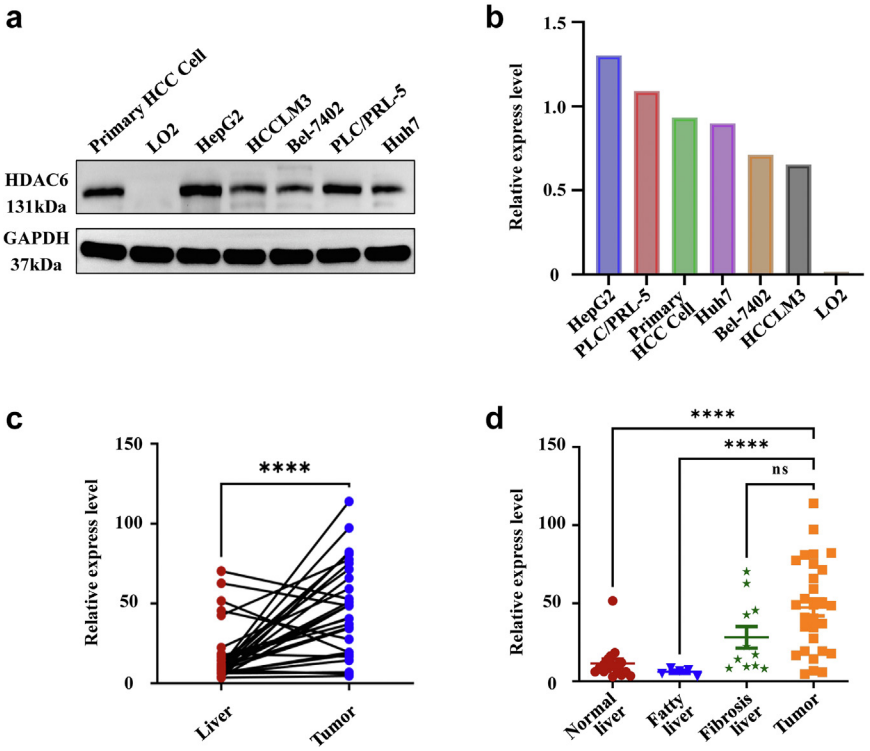

Fig. 1: **HDAC6 expression levels in cells and clinical patients**. (a ~ b) HDAC6 expression was generally up-regulated in liver cancer cells, with the highest expression in HepG2 and the lowest expression in HCCLM3. It was not expressed in LO2. (c) HDAC6 was overexpressed in samples from patients with liver cancer (n = 29). The relative expression level was statistically different (****$p < 0.0001$, Paired t-test). (d) The expression of HDAC6 in HCC (n = 29) was significantly higher than that in normal liver (n = 17) and fatty liver (n = 5) (****$p < 0.0001$) (Student's t-test), but not in liver fibrosis (n = 11) (Multiple comparisons).

assess the differential expression of HDAC6. The findings revealed that HDAC6 expression was markedly higher in HCC compared to normal liver and fatty liver (****$p < 0.0001$, *Student's t-test*), but there was no significant difference observed in liver fibrosis (Fig. 1d).

Synthesis of $SeCF_3$-IRD800

The synthetic route of probe $SeCF_3$-IRD800 is depicted in Fig. S1. First of all, intermediate **1** as the starting material,[52] which was prepared according to our previous reports, was reacted with (trifluoromethyl)trimethylsilane ($TMSCF_3$) under the catalysis of tetrabutylammonium (TBAF) fluoride to obtain compound **2**. Subsequently, the protecting group Boc of **2** was removed by trifluoroacetic acid (TFA), affording the key intermediate **3**. Finally, the probe IRDye800cw-$SeCF_3$ was accomplished by conjugating IRDye800cw-NHS with intermediate **3**.

Characterization of $SeCF_3$-IRD800

The spectroscopic properties of $SeCF_3$-IRD800 were initially evaluated. The excitation spectra peak of $SeCF_3$-IRD800 was 773 nm (Fig. 2a). The peak of the absorption spectra appeared at 803 nm (Fig. 2b). The fluorescence signal of $SeCF_3$-IRD800 was still present in the NIR-II window above 1000 nm and the emission spectrum peak was 803 nm (Fig. 2c, local amplification), which gradually weakened with the increase of the NIR-II filter wavelength (Fig. 2d). The results indicated that $SeCF_3$-IRD800 could be used for NIR-II fluorescence imaging.

To evaluate the bio-imaging capability of $SeCF_3$-IRD800, NIR-II fluorescence imaging experiments were carried out *in vitro*. In the imaging experiments, the 808 laser was used as the excitation source because of its widespread availability and low biological absorption. As shown in Fig. 2e, the fluorescence intensity of $SeCF_3$-IRD800 at different concentrations was detected, and the NIR-II fluorescence intensity of $SeCF_3$-IRD800 is linearly related to the concentration within a certain range. The fluorescence intensity of simple dyes IRDye800cw and $SeCF_3$-IRD800 varied with the concentration in different solvents. The fluorescence intensity of the fetal bovine serum (FBS) group was higher than that of the PBS group, and the fluorescence intensity of IRDye800cw was higher than that of $SeCF_3$-

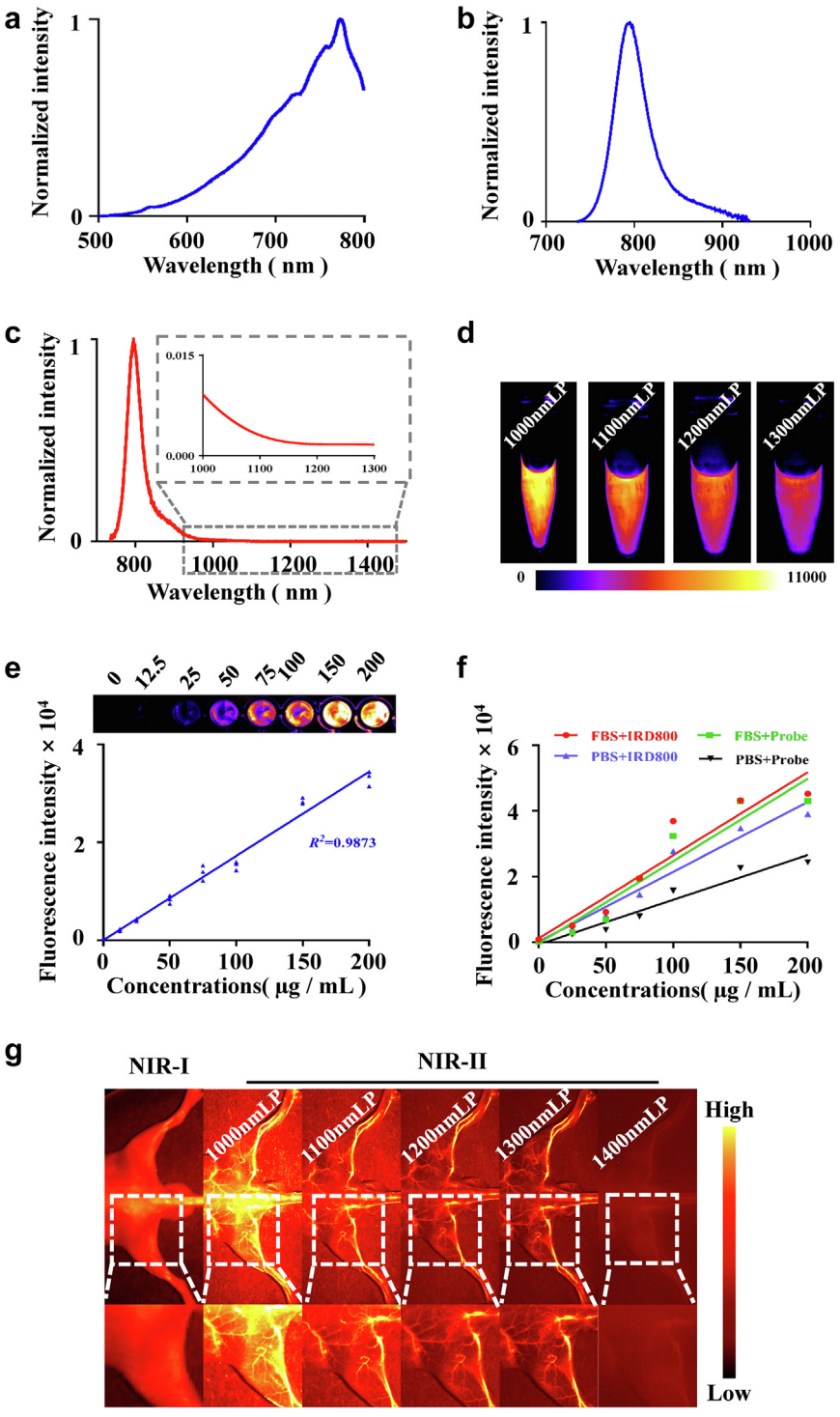

Fig. 2: **Characterization of $SeCF_3$-IRD800**. (a ~ b) Excitation spectra, and absorption spectra after signal intensity normalization. (c) Emission spectra in NIR-II spectra. (d) Fluorescence intensity under different NIR-II filters. (e) The NIR-II fluorescence intensity of $SeCF_3$-IRD800 is linearly related to the concentration within a certain range (R^2 = 0.9873, Simple linear regression). (f) The type of solvent affected the fluorescence intensity of $SeCF_3$-IRD800, the fluorescence intensity of the simple dye IRDye800cw is higher than that of $SeCF_3$-IRD800. (g) $SeCF_3$-IRD800 NIR-II imaging of blood vessels. Imaging filter:1000 nmLP. Exposure time:300 ms. Excitation wavelength:808 nm. Laser power density: 21.10 mW/cm^2. Imaging field of view: 10 cm.The type of camera sensor: InGaAs.

IRD800 (Fig. 2f), indicating that the imaging efficiency of $SeCF_3$-IRD800 was significantly improved after it was dispersed in blood. Compared to NIR-I and NIR-II mouse vascular imaging, NIR-II has significant advantages in imaging resolution and signal-to-noise ratio (Fig. 2g).

Toxicity of IRDye800cw-$SeCF_3$ in cell lines and normal Balb/c nude mice

The cytotoxicity of $SeCF_3$-IRD800 was evaluated on normal liver cell line LO2, and HCC cell lines (HepG2-luc, HCCLM3-luc) using CCK8 assays. $SeCF_3$-IRD800 had no toxicity to the above 3 cell lines at the concentration of 0∼280 μg/mL, and the cell survival rate was still above 90% even at a high concentration of 280 μg/mL (Fig. S2a–c). No obvious toxic effects were observed especially in normal cells, and the cell survival rate was above 95%.

The biocompatibility of $SeCF_3$-IRD800 was evaluated in normal Balb/c nude mice. Dissolve 200 nmol $SeCF_3$-IRD800 in 100 uL PBS (M&C GENE Technology (Beijing) Ltd.) and inject into healthy nude mice. Liver and kidney functions were assessed after 3 days (n = 3) and 30 days (n = 3) of injection, and the results demonstrated no detrimental effects caused by $SeCF_3$-IRD800 on these functions (Table S2). Additionally, major organs including hearts, livers, spleens, lungs, and kidneys were extracted for pathological analysis (Fig. S2d). The findings revealed no observable pathological changes or significant toxic effects induced by $SeCF_3$-IRD800 on these organs.[32]

Based on these results, it can be concluded that $SeCF_3$-IRD800 exhibits excellent biosafety and holds great potential for various *in vivo* biomedical imaging applications.

In vivo and *Ex vivo* NIR-II imaging

To demonstrate the metabolic characteristics of $SeCF_3$-IRD800, we intravenously injected $SeCF_3$-IRD800 and ICG into HepG2-luc tumor-bearing nude mice (n = 6, respectively). Subsequently, self-developed closed-field NIR-II fluorescence imaging equipment was used to observe the NIR-II fluorescence signal. The tumor-bearing mice were imaged using NIR-II 1000 nm long pass filters.

In the $SeCF_3$-IRD800 group (red line), we observed NIR-II fluorescence signal in the tumor area at 2 h, which gradually increased and reached its peak at 8 h (7658.41 ± 933.34) (Fig. 3a). This peak was associated with the highest TBR of 5.20 ± 1.04 (Fig. 3b and c). Subsequently, the fluorescence signal weakened over time. Nevertheless, the ICG group (blue line) exhibited a low level of tumor fluorescence signal within 48 h. The fluorescence intensity and TBR of the ICG group were significantly different from those of the $SeCF_3$-IRD800 group, as confirmed by the student's t-test. The $SeCF_3$-IRD800 group showed a rapid decline in liver region fluorescence intensity. At 48 h, the average fluorescence intensity in the ICG group was 2416.86 ± 769.67. There was a significant difference in fluorescence intensity between the two groups at each time point within the 48 h (**$p < 0.05$, Paired t-test) (Fig. 3d).

Ex vivo color and NIR-II imaging of organs after intravenous injection 8 h to show the biodistribution of $SeCF_3$-IRD800 (n = 4) (Fig. S3a and b). The fluorescence signal of the tumor was much higher than that of all major organs in mice, the low fluorescence signal was observed in the liver area, indicating that $SeCF_3$-IRD800 could be rapidly metabolized *in vivo* through the kidneys. This result also confirmed the small-molecule property of $SeCF_3$-IRD800. The uptake of $SeCF_3$-IRD800 by tumors was significantly higher than that of other *ex vivo* organs (Fig. S3c), and all were statistically significant (****$p < 0.0001$, Multiple comparison). Further study of the tumor and major organs to liver intensity ratio (Fig. S3d). The fluorescence signal ratios of the tumor and organs to the liver were further quantified and there were significant differences (****$p < 0.0001$, Multiple comparison). Tumor to liver ratio (TLR) was used to describe the differentiation of fluorescence intensity of tumors compared with the liver. The highest TLR was 10.97, and the average TLR was 6.86 ± 3.28 (Fig. S3d). These data indicated that $SeCF_3$-IRD800 could easily distinguish tumors from other organs, and had a promising application prospect in fluorescent navigation surgery for liver cancer.

In vivo targeting experiments

To evaluate the targeting ability *in vivo*, NIR-II imaging at different time points of intravenous injection $SeCF_3$-IRD800 in HepG2-Luc and HCCLM3 subcutaneous xenograft tumor models (n = 12) and in HepG2-Luc subcutaneous tumor blocking experiments (n = 6) were carried out. As shown in Fig. 4a, the average fluorescence intensity of the Imaging HCCLM3 group and Blocking HepG2 group was lower than that of the Imaging HepG2-Luc group at all time points. Notably, the optimal observation time was determined to be 8 h after injection (Fig. 4b). The average fluorescence intensity for the 3 groups was measured as follows: Imaging HepG2 group (15,029.12 ± 1841.44), Imaging HCCLM3 group (11,216.16 ± 975.70), and Blocking HepG2 group (5542.80 ± 1452.13) (***$p < 0.001$, Student's t-test). The TBR values for the Imaging HepG2-Luc group, Imaging HCCLM3 group, and Blocking HepG2 group were determined as 4.55 ± 0.49, 3.04 ± 0.78, and 0.98 ± 0.37, respectively (***$p < 0.001$, Student's t-test) (Fig. 4c). The results strongly indicated that $SeCF_3$-IRD800 exhibits *in vivo* targeting capabilities for HDAC6-positive HCC tumor cells, enabling efficient identification of HDAC6-positive tumor cells.

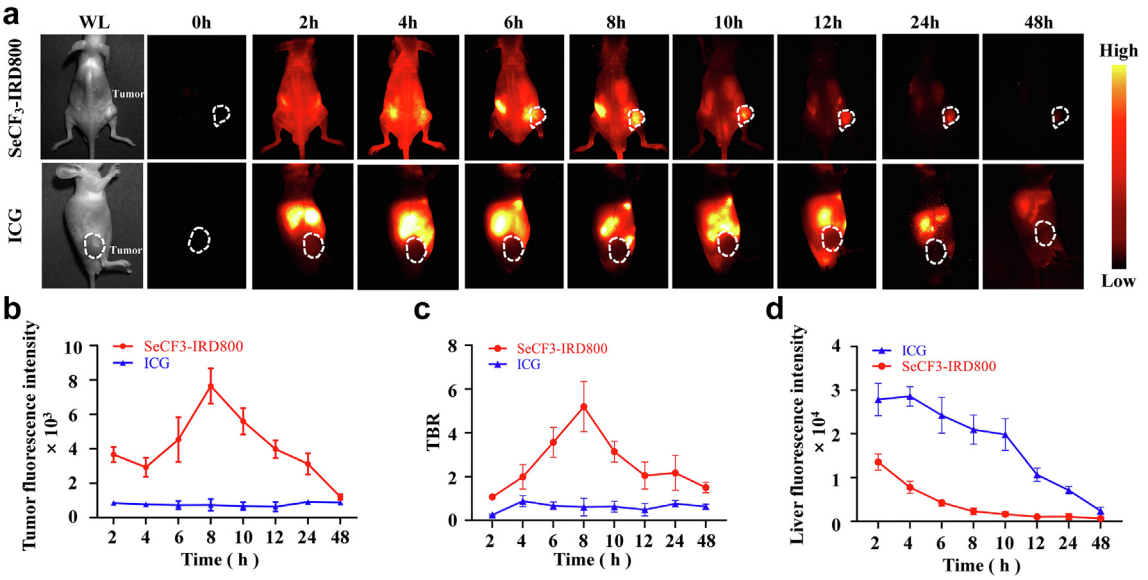

***Fig. 3: In vivo* NIR-II imaging and biodistribution of $SeCF_3$-IRD800 for subcutaneous tumor-bearing mice.** (a) *In vivo* imaging of $SeCF_3$-IRD800 and ICG. The tumor fluorescence signal acquisition area is shown in the white dotted line box on the right side of mice. (b ~ c) Quantitative analysis of fluorescence intensity and TBR over 48 h. The fluorescence intensity of tumors increased gradually after injection of $SeCF_3$-IRD800 and reached the highest fluorescence intensity and the best TBR at 8 h (7658.41 ± 933.34, 5.20 ± 1.04, respectively) (Red line). ICG accumulates in the liver and the tumor has no fluorescence signal. (Blue line) (d) Comparison of liver fluorescence signals between $SeCF_3$-IRD800 and ICG imaging ($SeCF_3$-IRD800: Red line. ICG: Blue line). Imaging filter:1000 nmLP. Exposure time:300 ms. Excitation wavelength:808 nm. Laser power density: 21.10 mW/cm^2. Imaging field of view: 10 cm. The type of camera sensor: InGaAs.

NIR-II fluorescence-guided HCC surgery

Radical resection of liver cancer is the only possible curative method for patients with HCC, and fluorescent targeting probes can be supplemented to achieve accurate and comprehensive resection of tumors. Based on previous *in vivo* imaging results, the fluorescence-guided resection effect of $SeCF_3$-IRD800 was further carried out under the fluorescence guidance of NIR-II on liver cancer *in situ*. As shown in Fig. 5, IVIS CT-BLI reconstruction showed the 3D location of the tumor (Fig. 5b), and subsequently, the mouse abdomen was dissected open to expose the liver, the procedure of fluorescent-guided surgery is shown in Fig. 5c. Then the tumor was removed visually, but strong fluorescence was still present in the surrounding area detected by NIR-II. Thus, the fluorescence area was further resected. HE staining confirmed that the residual lesion was a tumor (Fig. 5e). In addition, the fluorescence intensities of the tumor and liver area were recorded during the operation and were statistically significant (****$p < 0.0001$, Student's t-test) (Fig. 5d). The results proved that the tumor and normal liver area could be accurately distinguished by the fluorescence guidance of NIR-II to satisfy the clinical application need for complete HCC tumor resection.

Interestingly, during the experiment, an *in-situ* mouse did not show any tumor lesions under white light with exposed liver (Fig. 6a). However, it was found to exhibit strong signals in both BLI and NIR-II (Fig. 6b and c). Subsequently, NIR-II fluorescence-guided surgery was performed until the mice showed no BLI and NIR-II fluorescence. Removing cancer tissues were further subjected to NIR-II imaging and HE staining. The results showed that the maximum diameters of the tumor fluorescence areas were 2.0 mm and 2.5 mm, respectively (Fig. 6d). The corresponding resected tissues were confirmed to be tumors by HE staining (Fig. 6e and f). The findings reveal that $SeCF_3$-IRD800 can assist surgeons in detecting sub-2.0 mm microscopic lesions that are invisible under white light and can also effectively identify tumor margins under NIR-II fluorescence guidance.

More than half of patients with HCC have a background of liver fibrosis or cirrhosis.[2,4] To evaluate the imaging effect of the $SeCF_3$-IRD800 in various pathological backgrounds, we conducted NIR-II imaging on mice with liver fibrosis (n = 6) and mice with *in situ* liver tumors (n = 6). NIR-II imaging was performed 8 h after intravenous injection, allowing for visualization of the mice above (Fig. 7a). Pathology histology analysis was conducted to validate the findings. Sirius Red staining was utilized to visualize fibrosis liver, indicated by collagen deposition (black arrow). Additionally, HE staining was performed to differentiate the tumor from normal liver, and IHC was used to quantify HDAC6 expression levels (Scale bars: 1000 μm, 50 μm) (Fig. 7b). Quantitative analysis was carried out on both the

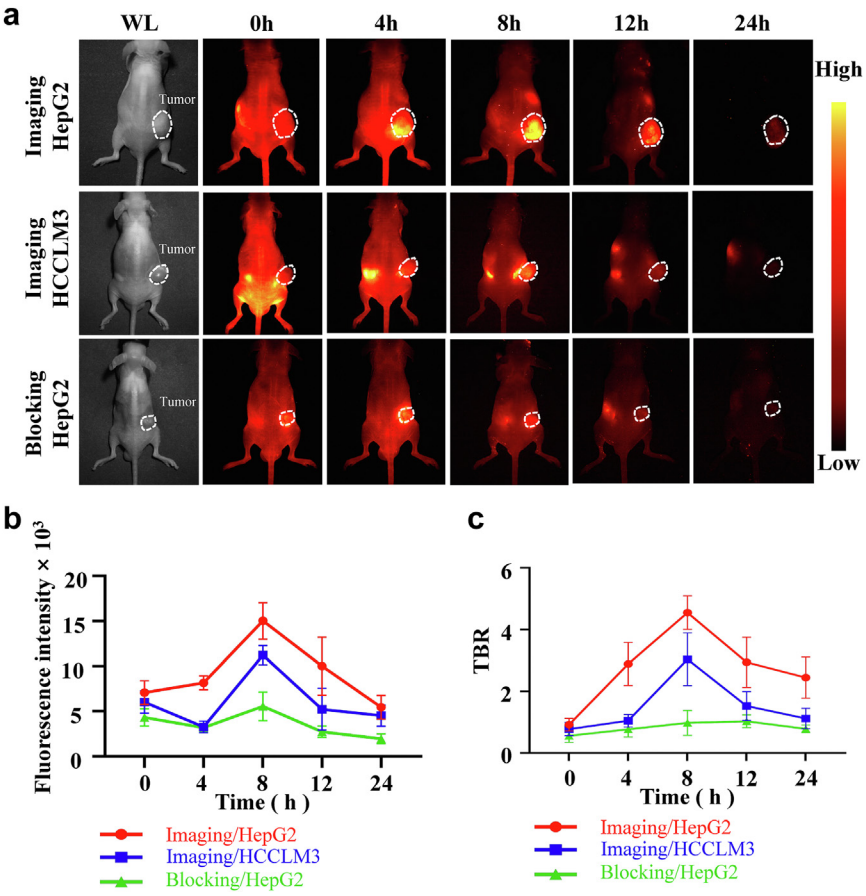

Fig. 4: In vivo* specificity of $SeCF_3$-IRD800**. (a) NIR-II imaging at different time points of intravenous injection $SeCF_3$-IRD800 in HepG2-Luc and HCCLM3 subcutaneous xenograft tumor models (n = 12) and HepG2-Luc subcutaneous tumor blocking experiments (n = 6). (b) Fluorescence intensity of tumor. Imaging HepG2 group (15,029.12 ± 1841.44), Imaging HCCLM3 group (11,216.16 ± 975.70), and Blocking HepG2 group (5542.80 ± 1452.13) ($p < 0.001$, Student's t-test). (c) Tumor-to-background ratio (TBR) of NIR-II fluorescence signal intensity and the skin fluorescence signal intensity around the tumor were selected as the background. Imaging HepG2 group, Imaging HCCLM3 group, and Blocking HepG2 group were determined as 4.55 ± 0.49, 3.04 ± 0.78, and 0.98 ± 0.37, respectively (***$p < 0.001$, Student's t-test). Imaging filter:1000 nmLP. Exposure time:300 ms. Excitation wavelength:808 nm. Laser power density: 21.10 mW/cm^2. Imaging field of view: 10 cm.The type of camera sensor: InGaAs.

fluorescence intensity and HDAC6 expression levels in the liver fibrosis and *in situ* liver cancer (n = 6) models (Fig. 7c and d). There is a statistically significant difference in fluorescence intensity and HDAC6 expression levels between fibrosis liver, normal liver, and tumor (*$p < 0.05$, Student's t-test). We further confirmed the correlation between fluorescence intensity and HDAC6 expression level (R^2 = 0.8124, Simple linear regression) (Fig. 7e).

Sample from patients with HCC incubation of $SeCF_3$-IRD800

Cancer and adjacent tissues from 3 patients were divided into 3 groups: Tumor/$SeCF_3$-IRD800 for the tumor imaging group, Tumor/SAHA/$SeCF_3$-IRD800 for the tumor blockade group, and Liver/$SeCF_3$-IRD800 for the liver imaging group. As shown in Fig. 8a, the fluorescence intensity of Tumor/$SeCF_3$-IRD800 was recognizable as higher than the other groups. IHC confirmed that the HDAC6 was highly expressed in tumors, but expressed at a lower level in the liver (Fig. 8b). Further quantitative analysis of fluorescence intensity (ImageJ, NIH, https://imagej.nih.gov/ij/) and HDAC6 expression levels (Image-Pro Plus 6.0) indicated that the fluorescence signal of the Tumor/SAHA/$SeCF_3$-IRD800 and Liver/$SeCF_3$-IRD800 was significantly lower than that of the tumor imaging group (****$p < 0.0001$, Student's t-test) (Fig. 8c). However, there was no significant difference in HDAC6 expression levels between the Tumor/SAHA/$SeCF_3$-IRD800 and Tumor/$SeCF_3$-IRD800, indicating that the difference in fluorescence intensity was due to HDAC6 blockade. The expression level of

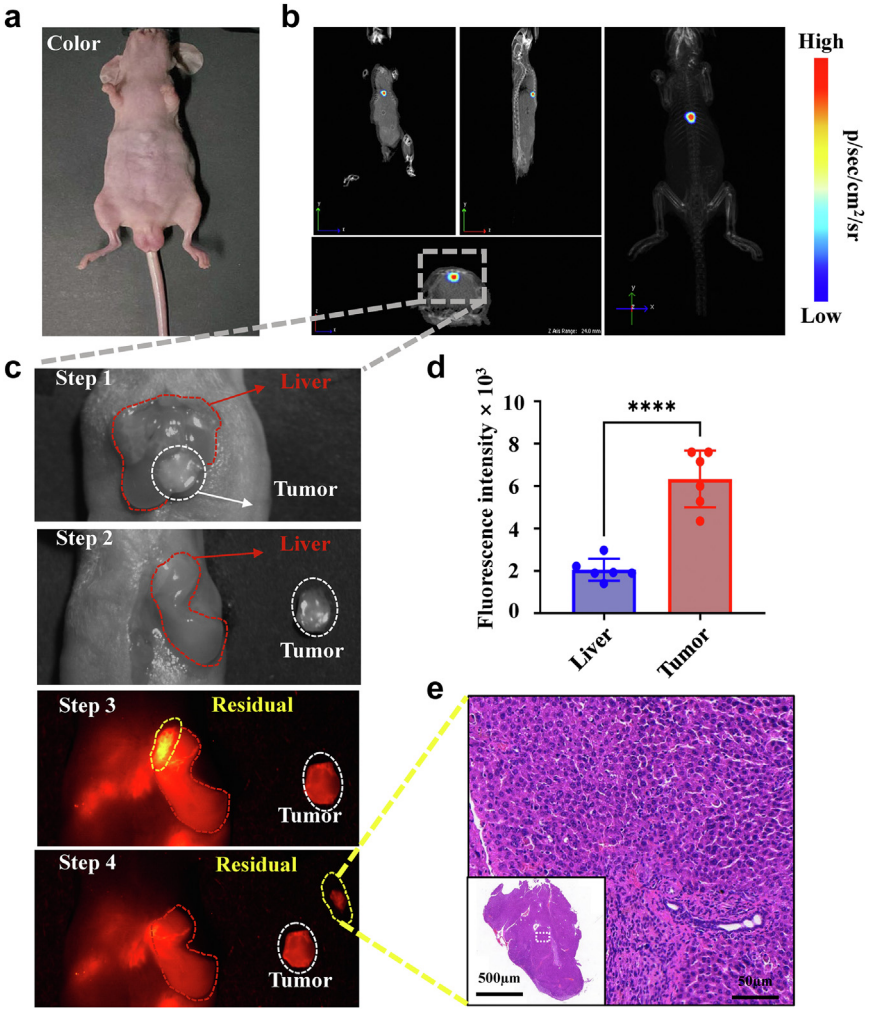

Fig. 5: **NIR-II fluorescence-guided surgery for HCC**. (a) Color imaging of the mice. (b) BLI-CT 3D reconstruction of the tumor. (Tumor area: Gray dashed wireframe) (c) Fluorescence-guided surgery process. Step 1: white light examination for HCC lesions. Step 2: first resection under white light. Step 3: NIR-II fluorescence-guided examination for residual lesions. Step 4: Removal of residual lesions. (d) Quantitative analysis of intraoperative fluorescence intensity in livers (blue) and tumors (red) (n = 6) (****$p < 0.0001$, Student's t-test). (e) Pathological results of all residual lesions (Scale bars: 500 μm, 50 μm, respectively). Imaging filter:1000 nmLP. Exposure time:300 ms. Excitation wavelength:808 nm. Laser power density: 21.10 mW/cm^2. Imaging field of view: 10 cm.The type of camera sensor: InGaAs.

HDAC6 in the Liver/$SeCF_3$-IRD800 was significantly lower than that in the Tumor/$SeCF_3$-IRD800 (***$p < 0.001$, Student's t-test), and the difference in fluorescence intensity was due to differences in the HDAC6 expression (Fig. 8d). These results suggest that $SeCF_3$-IRD800 has a specific targeting ability to HDAC6 and has great potential for clinical transformation in guiding tumor resection during liver cancer surgery.

Discussion

Surgical resection remains the primary therapeutic approach for hepatocellular carcinoma (HCC) and offers the potential for long-term benefits. However, challenges arise in accurately distinguishing HCC lesions from normal liver tissue due to subjective factors like visual diagnosis and palpation. Furthermore, preserving sufficient liver parenchyma is crucial for liver function and recovery of patients. Thus, the accurate intraoperative identification of HCC tissue to achieve complete tumor resection and reduce recurrence is pivotal for advancing HCC diagnosis and treatment. Fluorescence imaging has been a reliable tool for supporting surgical lesion identification and functional preservation for decades.[18] Specifically, near-infrared fluorescence imaging, notably NIR-II imaging, has been successfully applied to liver cancer fluorescence-guided surgery, yielding survival benefits for patients with HCC.[31]

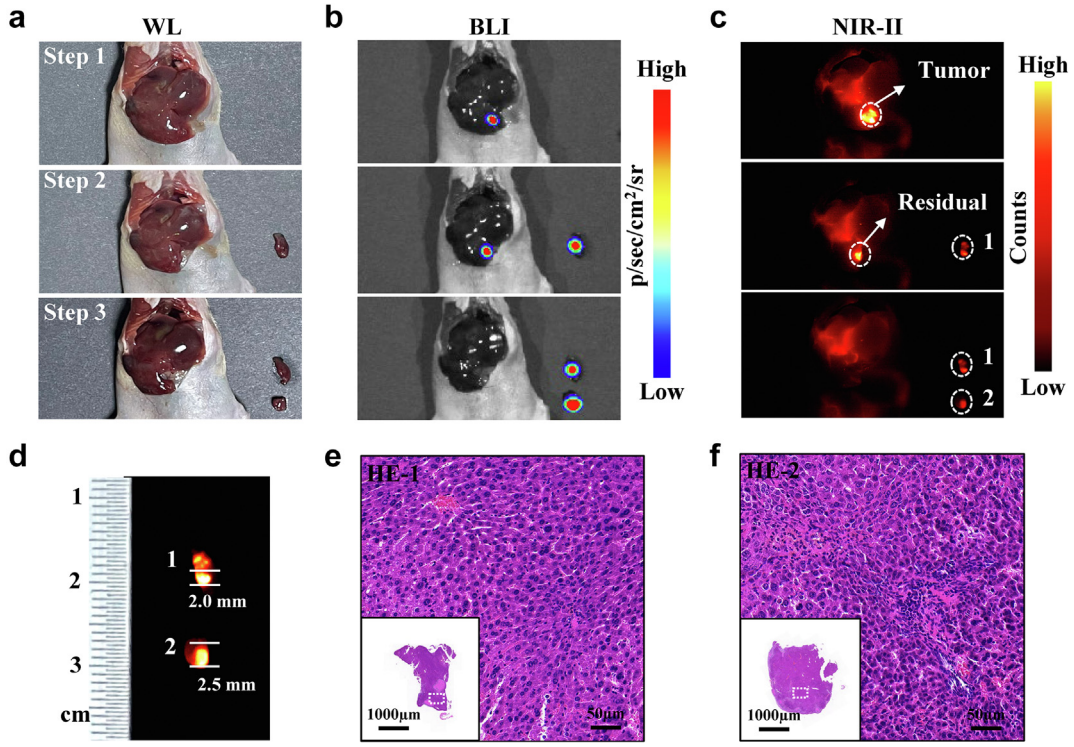

Fig. 6: **NIR-II intraoperative imaging of invisible liver cancer under white light**. (a ~ b) Color and BLI images during the surgery. Step 1: before resection. Step 2: first resection. Step 3: second resection. (c) NIR-II fluorescence-guided surgery process. The mouse was repeatedly imaged until no BLI signal was detected in the liver. (d) Size analysis for the 2 lesions. (e ~ f) Intraoperative HE staining of the above 2 lesions. (Scale bars: 1000 μm, 50 μm). Imaging filter:1000 nmLP. Exposure time:300 ms–1000 ms. Excitation wavelength:808 nm. Laser power density: 21.10 mW/cm^2. Imaging field of view: 10 cm.The type of camera sensor: InGaAs.

In recent years, significant progress has been made in NIR-I fluorescence-guided surgery (FGS). However, FDA-approved fluorescent dyes such as ICG, due to their non-specific accumulation within liver tissue, result in high background signals, particularly in liver cancer surgery originating from liver fibrosis or cirrhosis, where false-positive rates can reach 40%. In addition, IRDye800cw, a fluorescent dye proven through clinical trials, offers a longer emission wavelength compared to ICG, reducing tissue scattering and enhancing imaging quality. Enhanced stability and quantum yield allow it to maintain fluorescence signals at lower concentrations for extended periods, achieving excellent biocompatibility. Additionally, IRDye800cw has been shown to exhibit NIR-II tail signals, capturing fluorescence signals above 1000 nm, making it widely applicable in biomedical research.[53] Interestingly, small molecule fluorescent targeting probes can efficiently reduce the liver background signal and improve the tumor liver signal ratio (TLR).[45] Thus, the development of small-molecule fluorescent targeted probes may represent a crucial breakthrough in addressing the challenges of fluorescence-guided navigation in liver cancer surgery.

HDACs are a family of enzymes and play distinct roles in various stages of tumor initiation and progression. HDAC6, a subtype of HDACs, has been shown to contribute to carcinogenesis and regulate EMT in various cancers such as ovarian and breast cancers. Overexpression of HDAC6 is associated with anchorage-independent proliferation, tumor invasion, and carcinogenesis.[54,55] Although HDAC6 has been reported as a tumor suppressor inhibiting HCC development,[56] studies also indicate its potential for promoting tumor progression through inhibiting p53 transcriptional activity or enhancing HCC cell migration and invasion.[41,43] Currently, a range of HDAC6-specific targeted drugs has entered clinical trials, showing promising therapeutic effects.[57,58] In this study, HDAC6 immunohistochemical staining was performed on 29 HCC tissues and adjacent tissues, revealing significant expression differences with statistical significance (****$p < 0.0001$, paired t-test). Further inclusion of 4 cases of fatty liver tissues categorized the above tissues into liver cancer (n = 29), normal liver (n = 17), liver fibrosis (n = 11), and fatty liver (n = 5). Statistical analysis indicated statistically significant differences in HDAC6 expression between normal liver tissue and tumor tissue, as well as

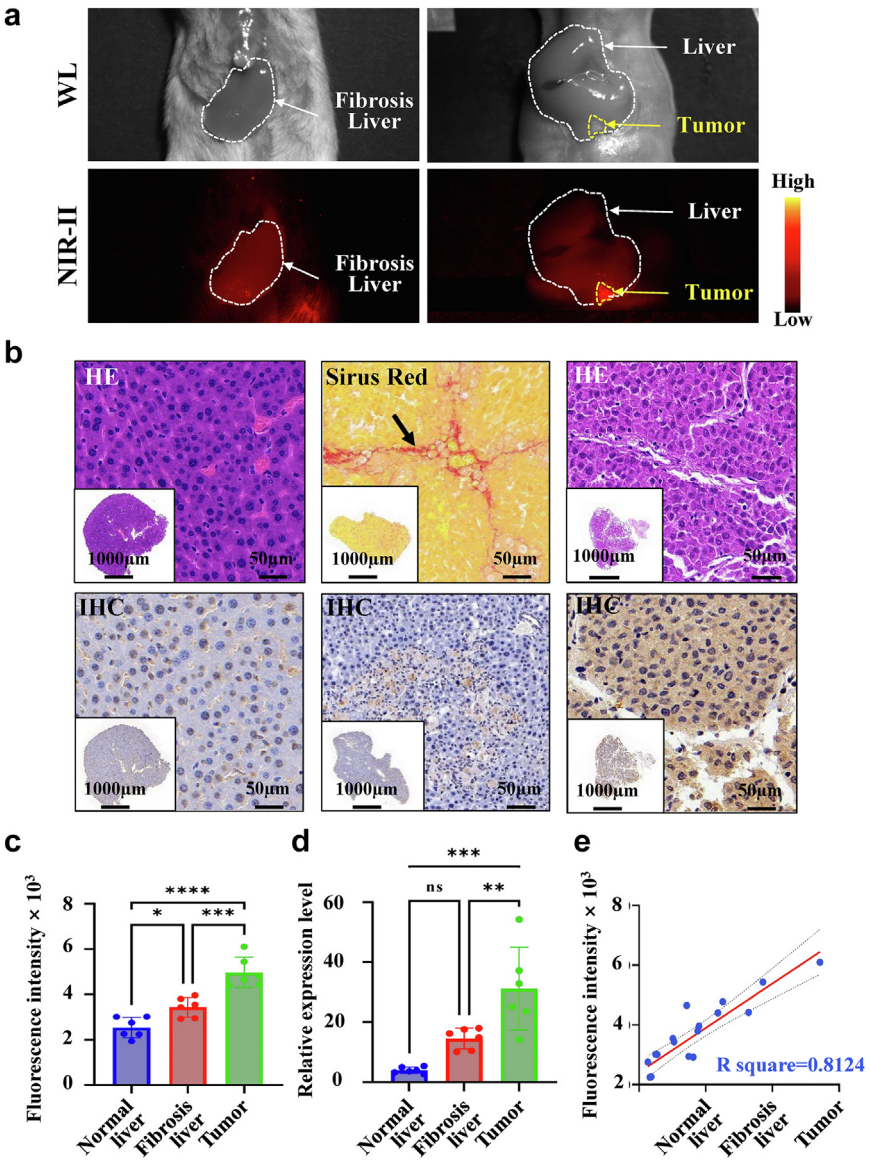

***Fig. 7*: Hepatic Fibrosis and *in-situ* Liver Cancer Imaging with $SeCF_3$-IRD800**. (a) NIR-II imaging of hepatic fibrosis (n = 6) and *in-situ* liver cancer (n = 6) at 8 h after intravenous injection. (b) Pathology histology analysis. Normal liver, fibrosis liver, and tumor left to right respectively. (HE staining: normal liver and tumor, Sirius red staining: fibrosis liver (black arrow, collagen deposition). IHC: HDAC6 expression levels among the above tissues). (c ~ d) Quantitative analysis of fluorescence intensity and HDAC6 expression level was performed in liver fibrosis (n = 6) and *in-situ* liver cancer (n = 6) models. (e) Correlation analysis between fluorescence intensity and HDAC6 expression in the above tissues (R^2 = 0.8124, Simple linear regression). Imaging filter:1000 nmLP. Exposure time:300 ms. Excitation wavelength:808 nm. Laser power density: 21.10 mW/cm^2. Imaging field of view: 10 cm. The type of camera sensor: InGaAs.

fatty liver tissue and tumor tissue (*****p < 0.0001*, Student's t-test). Interestingly, no significant difference was observed between liver fibrosis and liver cancer tissue, possibly due to the heterogeneity of liver cancer and sample size limitations. Therefore, HDAC6 can be regarded as a specific molecular marker for liver cancer imaging, facilitating precise surgical diagnosis and treatment by identifying HDAC6-positive liver cancer lesions intraoperatively.

In recent years, multi-modal imaging probes targeting HDACs for different tumors have been developed,[47] such as LBH589-Cy5.5[48] for breast cancer detection and 18 F-SAHA[59] for ovarian cancer detection. In terms of imaging modalities, nuclear imaging, and NIR-I

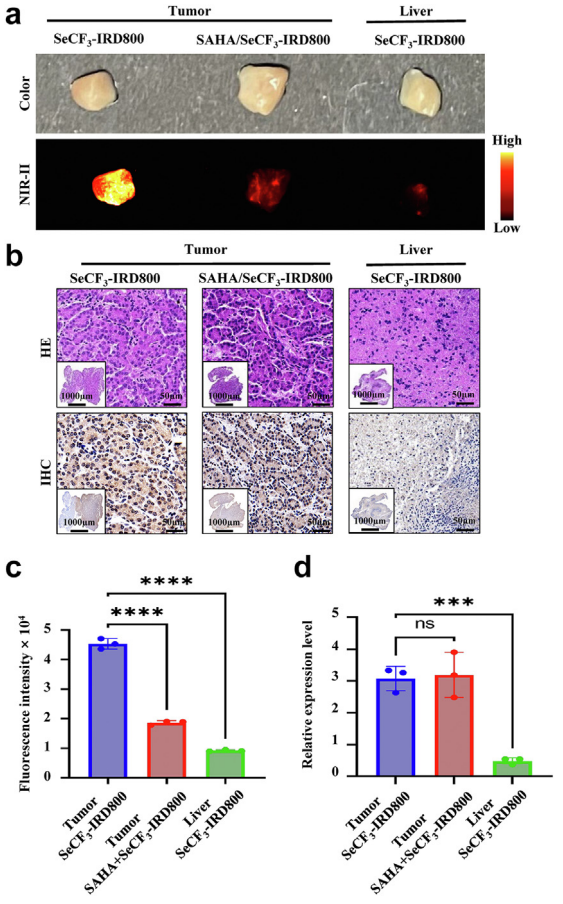

Fig. 8: **Incubation of samples from patients with HCC with $SeCF_3$-IRD800.** (a) Color and NIR-II imaging after incubation. Imaging filter: 1000 nmLP. Exposure time:300 ms. Excitation wavelength:808 nm. Laser power density: 21.10 mW/cm^2. Imaging field of view: 10 cm.The type of camera sensor: InGaAs. (b) HE staining and IHC after incubation with $SeCF_3$-IRD800. (Scale bars: 1000 μm and 50 μm, respectively) (c) Quantitative analysis of fluorescence intensity. Tumor/$SeCF_3$-IRD800 vs. Tumor/SAHA/$SeCF_3$-IRD800, Liver/$SeCF_3$-IRD800 (****$p < 0.0001$, ****$p < 0.0001$, respectively. Student's t-test). (d) Quantitative analysis of HDAC6 expression (Student's t-test). Tumor/$SeCF_3$-IRD800 vs. Tumor/SAHA/$SeCF_3$-IRD800(No significance, Student's t-test), Tumor/$SeCF_3$-IRD800 vs. Liver/$SeCF_3$-IRD800 (***$p < 0.001$, Student's t-test).

imaging have limited penetration depths, while NIR-II imaging can reach depths of up to 3 cm, providing deeper insights. Additionally, low imaging resolution limits the observation of fine structural details in samples. Moreover, nuclear and NIR-I imaging are susceptible to environmental light interference, leading to background noise. Most research in this area has focused on cancers such as ovarian and breast cancer, with relatively fewer studies on liver cancer intraoperative imaging, and many have targeted the HDAC family rather than specific subtypes, which might have implications for other physiological functions.

In this study, we labeled the trifluoromethyl-modified HDAC6 inhibitor 6 ($SeCF_3$) with IRDye800cw-NHS, designed, and synthesized a small-molecule fluorescent imaging probe targeted at the specific HDAC6 subtype, $SeCF_3$-IRD800. We applied this probe for *in vivo* NIR-II imaging, demonstrating its rapid kidney metabolism, specific accumulation in tumor regions, low liver fluorescence signal compared to tumor regions, and successful mitigation of the high liver fluorescence background signal issue inherent to fluorescence imaging. $SeCF_3$-IRD800 proves valuable for HCC and FGS fluorescence imaging, showing excellent biocompatibility. *In vivo* NIR-II imaging indicated that after 2 h of $SeCF_3$-IRD800 intravenous injection, fluorescence appeared in the tumor region, reaching maximum fluorescence intensity and TBR at 8 h. The optimal imaging time exhibited tumor fluorescence signals (7658.41 ± 933.34) and high TBR (5.20 ± 1.04). Additionally, imaging experiments with various expression levels demonstrated its HDAC6-specific targeting capability in multiple HCC tumor models, suitable for NIR-II intraoperative imaging. The feasibility of fluorescence-guided surgery was confirmed, enabling the detection of sub-2 mm tumor lesions under white light, and facilitating surgical decision-making. Further imaging of liver fibrosis mice demonstrated that $SeCF_3$-IRD800's imaging efficacy remains unaffected by liver pathological conditions. The correlation between HDAC6 expression levels and corresponding fluorescence intensities ($R^2 = 0.8124$) in HCC, liver fibrosis, and normal liver tissue was observed. $SeCF_3$-IRD800 identified HDAC6-positive human liver cancer specimens, presenting advantages in intraoperative identification during liver cancer surgery. Thus, the rapidly metabolized small-molecule NIR-II fluorescence probe targeting HDAC6, $SeCF_3$-IRD800, holds significant clinical translational value.

Currently, several targeted probes for different biomarkers have entered clinical trials. However, these probes, combined with monoclonal antibodies, exhibit prolonged *in vivo* distribution and metabolism times, accumulating in the liver and causing excessive background noise, which makes them less suitable for liver tumor imaging.[60–62] The combination of a small-molecule compound targeting HDAC6 and a fluorescent dye, as achieved in this study, effectively avoids liver fluorescence signals. $SeCF_3$-IRD800 injection achieves optimal imaging within 8 h, delivering high tumor fluorescence signals with a low fluorescence background signal. This provides a new solution for the clinical translation of liver cancer-targeted probes.

This study still presents limitations. First, our study represents preliminary application experiments for $SeCF_3$-IRD800, focusing on "feasibility" and "how to use," without investigating its sensitivity and surgical margins. Second, although SAHA has a drug half-life of approximately 10 h,[57,58] we did not

determine the blood half-life of $SeCF_3$-IRD800. A prolonged half-life might pose risks of adverse effects. Moreover, subjective bias may exist in fluorescence signal and background signal acquisition, potentially causing selection bias. However, due to tumor heterogeneity and individual differences in tumor size and target expression, the imaging results might be influenced. Lastly, limitations in animal models led to the absence of imaging evidence for HCC models stemming from hepatic fibrosis, weakening the imaging efficacy evidence for liver fibrosis, normal liver, and liver cancer. In FGS, limitations in operator manipulation and mouse liver size prevent complete simulation of clinical liver cancer curative resection, resulting in limited tumor edge detection. Tumor animal models still cannot fully replicate the tumor biological performance of patients with liver tumors, neglecting the impact of the primary tumor microenvironment on metabolism.

In summary, we successfully designed and synthesized the NIR-II probe $SeCF_3$-IRD800, targeting HDAC6 for liver cancer imaging and fluorescence-guided surgery. This probe enables precise *in vivo* HDAC6-targeted imaging of liver cancer and rapidly metabolizes through the kidneys, achieving optimal imaging at 8 h. Imaging remains unaffected by liver pathological conditions, initiating preliminary exploration of fluorescence-guided surgery and detecting sub-2 mm microtumor lesions invisible under white light. Clinical tissue incubation experiments also revealed its specific binding capability to clinical tissue samples. Therefore, $SeCF_3$-IRD800 can be used for detecting HDAC6 expression levels in tumors, liver cancer targeted imaging, NIR-II fluorescence-guided liver cancer surgery, and identifying clinical HDAC6-positive liver cancer tissue, offering significant clinical translational value and promising clinical prospects.

Contributors

Study design: Tian Jie, Zhenhua Hu, Jian Li, Xiaohua Jia.

Literature search: Bo Wang, Xiaohua Jia, Xiaoyong Guo, Qiyue Yang.

Data collection: Bo Wang, En Lin, Ganyuan Xie, Chu Tang, Caiguang Cao, Xiaojing Shi.

Data analysis: all authors.

Data interpretation: all authors.

Figures: Bo Wang, Xiaoyong Guo, Peiping Li, Decheng Li, Baojia Zou.

Writing: Bo Wang, En Lin, Xiaoyong Guo, Chu Tang.

Revise Bo Wang, Xiaohua Jia, Chu Tang, Jian Li, Chaonong Cai.

Access and verification of the data: all authors.

Responsibilities for the decision to submit the manuscript: all authors.

All authors reviewed, discussed, and agreed with the manuscript.

Data sharing statement

The main data supporting the results of this study are available within the paper and its Supplementary materials. The raw near-infrared fluorescence images can be obtained after asking the corresponding authors and clarifying the purpose of use.

Declaration of interests

The authors declare that they have no conflicts of interest.

Acknowledgements

This paper is supported by the National Natural Science Foundation of China (NSFC) (92059207, 62027901, 81930053, 81227901, 82272105, U21A20386 and 81971773), CAS Youth Interdisciplinary Team (JCTD-2021-08), the Zhuhai High-level Health Personnel Team Project (Zhuhai HLHPTP201703), and Guangdong Basic and Applied Basic Research Foundation under Grant No. 2022A1515011244.

The authors would like to thank Hongguang Wang and Xuan Meng from the Department of Hepatobiliary Surgery, Cancer Hospital of the Chinese Academy of Medical Sciences for their great assistance in collecting clinical samples.

We would like to thank Professor Zhen Cheng from the Center for Molecular Imaging, Shanghai Institute of Materia Medica, Chinese Academy of Sciences, for his guidance on study design and implementation.

Appendix A. Supplementary data

Supplementary data related to this article can be found at https://doi.org/10.1016/j.ebiom.2023.104880.

References

1 Sung H, Ferlay J, Siegel RL, et al. Global cancer statistics 2020: GLOBOCAN estimates of incidence and mortality worldwide for 36 cancers in 185 countries. *CA A Cancer J Clin*. 2021;71(3):209–249.
2 Forner A, Reig M, Bruix J. Hepatocellular carcinoma. *Lancet*. 2018;391(10127):1301–1314.
3 Torzilli G, Belghiti J, Kokudo N, et al. A snapshot of the effective indications and results of surgery for hepatocellular carcinoma in tertiary referral centers: is it adherent to the EASL/AASLD recommendations?: an observational study of the HCC East-West study group. *Ann Surg*. 2013;257(5):929–937.
4 Llovet JM, Kelley RK, Villanueva A, et al. Hepatocellular carcinoma. *Nat Rev Dis Primers*. 2021;7(1):6.
5 Yim SY, Park BJ, Um SH, et al. Diagnostic performance of gadoxetic acid (Primovist)-enhanced MR imaging versus CT during hepatic arteriography and portography for small hypervascular hepatocellular carcinoma. *Medicine (Baltim)*. 2016;95(39):e4903.
6 Nguyen QT, Tsien RY. Fluorescence-guided surgery with live molecular navigation–a new cutting edge. *Nat Rev Cancer*. 2013;13(9):653–662.
7 Zhong L, Dong D, Fang X, et al. A deep learning-based radiomic nomogram for prognosis and treatment decision in advanced nasopharyngeal carcinoma: a multicentre study. *eBioMedicine*. 2021;70:103522.
8 Yang W, Qin W, Hu Z, et al. Comparison of Cerenkov luminescence imaging (CLI) and gamma camera imaging for visualization of let-7 expression in lung adenocarcinoma A549 Cells. *Nucl Med Biol*. 2012;39(7):948–953.
9 Cai M, Zhang Z, Shi X, Yang J, Hu Z, Tian J. Non-Negative iterative convex refinement approach for accurate and robust reconstruction in cerenkov luminescence tomography. *IEEE Trans Med Imaging*. 2020;39(10):3207–3217.
10 Zheng S, Zhang Z, Qu Y, et al. Radiopharmaceuticals and fluorescein sodium mediated triple-modality molecular imaging allows precise image-guided tumor surgery. *Adv Sci*. 2019;6(13):1900159.
11 Shi X, Zhang Z, Zhang Z, et al. Near-infrared window II fluorescence image-guided surgery of high-grade gliomas prolongs the progression-free survival of patients. *IEEE Trans Biomed Eng*. 2022;69(6):1889–1900.
12 Liu M, Zheng S, Zhang X, et al. Cerenkov luminescence imaging on evaluation of early response to chemotherapy of drug-resistant gastric cancer. *Nanomedicine*. 2018;14(1):205–213.
13 Hu Z, Chen X, Liang J, et al. Single photon emission computed tomography-guided Cerenkov luminescence tomography. *J Appl Phys*. 2012;112(2).

14 Ishizawa T, Fukushima N, Shibahara J, et al. Real-time identification of liver cancers by using indocyanine green fluorescent imaging. *Cancer*. 2009;115(11):2491–2504.
15 Gotoh K, Yamada T, Ishikawa O, et al. A novel image-guided surgery of hepatocellular carcinoma by indocyanine green fluorescence imaging navigation. *J Surg Oncol*. 2009;100(1):75–79.
16 Ishizawa T, Masuda K, Urano Y, et al. Mechanistic background and clinical applications of indocyanine green fluorescence imaging of hepatocellular carcinoma. *Ann Surg Oncol*. 2014;21(2):440–448.
17 Terasawa M, Ishizawa T, Mise Y, et al. Applications of fusion-fluorescence imaging using indocyanine green in laparoscopic hepatectomy. *Surg Endosc*. 2017;31(12):5111–5118.
18 Lauwerends LJ, van Driel P, Baatenburg de Jong RJ, et al. Real-time fluorescence imaging in intraoperative decision making for cancer surgery. *Lancet Oncol*. 2021;22(5):e186–e195.
19 Wang X, Teh CSC, Ishizawa T, et al. Consensus guidelines for the use of fluorescence imaging in hepatobiliary surgery. *Ann Surg*. 2021;274(1):97–106.
20 Ishizawa T, Zuker NB, Kokudo N, Gayet B. Positive and negative staining of hepatic segments by use of fluorescent imaging techniques during laparoscopic hepatectomy. *Arch Surg*. 2012;147(4):393–394.
21 He K, Hong X, Chi C, et al. Efficacy of near-infrared fluorescence-guided hepatectomy for the detection of colorectal liver metastases: a randomized controlled trial. *J Am Coll Surg*. 2022;234(2):130–137.
22 Zhang Z, He K, Chi C, Hu Z, Tian J. Intraoperative fluorescence molecular imaging accelerates the coming of precision surgery in China. *Eur J Nucl Med Mol Imaging*. 2022;49(8):2531–2543.
23 Takasaki K. Glissonean pedicle transection method for hepatic resection: a new concept of liver segmentation. *J Hepatobiliary Pancreat Surg*. 1998;5(3):286–291.
24 Cho A, Okazumi S, Makino H, et al. Relation between hepatic and portal veins in the right paramedian sector: proposal for anatomical reclassification of the liver. *World J Surg*. 2004;28(1):8–12.
25 Kaibori M, Ishizaki M, Matsui K, Kwon AH. Intraoperative indocyanine green fluorescent imaging for prevention of bile leakage after hepatic resection. *Surgery*. 2011;150(1):91–98.
26 Kubota K, Kita J, Shimoda M, et al. Intraoperative assessment of reconstructed vessels in living-donor liver transplantation, using a novel fluorescence imaging technique. *J Hepatobiliary Pancreat Surg*. 2006;13(2):100–104.
27 Coubeau L, Frezin J, Dehon R, Lerut J, Reding R. Indocyanine green fluoroscopy and liver transplantation: a new technique for the intraoperative assessment of bile duct vascularization. *Hepatobiliary Pancreat Dis Int*. 2017;16(4):440–442.
28 Marino MV, Podda M, Fernandez CC, Ruiz MG, Fleitas MG. The application of indocyanine green-fluorescence imaging during robotic-assisted liver resection for malignant tumors: a single-arm feasibility cohort study. *HPB (Oxford)*. 2020;22(3):422–431.
29 Lu G, van den Berg NS, Martin BA, et al. Tumour-specific fluorescence-guided surgery for pancreatic cancer using panitumumab-IRDye800CW: a phase 1 single-centre, open-label, single-arm, dose-escalation study. *Lancet Gastroenterol Hepatol*. 2020;5(8):753–764.
30 Antaris AL, Chen H, Diao S, et al. A high quantum yield molecule-protein complex fluorophore for near-infrared II imaging. *Nat Commun*. 2017;8:15269.
31 Hu Z, Fang C, Li B, et al. First-in-human liver-tumour surgery guided by multispectral fluorescence imaging in the visible and near-infrared-I/II windows. *Nat Biomed Eng*. 2020;4(3):259–271.
32 Chang B, Li D, Ren Y, et al. A phosphorescent probe for in vivo imaging in the second near-infrared window. *Nat Biomed Eng*. 2022;6(5):629–639.
33 Zhu S, Tian R, Antaris AL, Chen X, Dai H. Near-infrared-II molecular dyes for cancer imaging and surgery. *Adv Mater*. 2019;31(24):e1900321.
34 Antaris AL, Chen H, Cheng K, et al. A small-molecule dye for NIR-II imaging. *Nat Mater*. 2016;15(2):235–242.
35 Hu Z, Qu Y, Wang K, et al. In vivo nanoparticle-mediated radiopharmaceutical-excited fluorescence molecular imaging. *Nat Commun*. 2015;6:7560.
36 Zhang Z, Fang C, Zhang Y, et al. NIR-II nano fluorescence image guided hepatic carcinoma resection on cirrhotic patient. *Photodiagnosis Photodyn Ther*. 2022;40:103098.
37 Cao C, Deng S, Wang B, et al. Intraoperative near-infrared II window fluorescence imaging-assisted nephron-sparing surgery for complete resection of cystic renal masses. *Clin Transl Med*. 2021;11(10):e604.
38 Jyab F, Shc G, Zhb E, et al. In vivo multifunctional fluorescence imaging using liposome-coated lanthanide nanoparticles in near-infrared-II/IIa/IIb windows. 2021;38:101120.
39 Hesham HM, Lasheen DS, Abouzid KAM. Chimeric HDAC inhibitors: comprehensive review on the HDAC-based strategies developed to combat cancer. *Med Res Rev*. 2018;38(6):2058–2109.
40 Lv Z, Weng X, Du C, et al. Downregulation of HDAC6 promotes angiogenesis in hepatocellular carcinoma cells and predicts poor prognosis in liver transplantation patients. *Mol Carcinog*. 2016;55(5):1024–1033.
41 Kanno K, Kanno S, Nitta H, et al. Overexpression of histone deacetylase 6 contributes to accelerated migration and invasion activity of hepatocellular carcinoma cells. *Oncol Rep*. 2012;28(3):867–873.
42 Tang C, Li C, Zhang S, et al. Novel bioactive hybrid compound dual targeting estrogen receptor and histone deacetylase for the treatment of breast cancer. *J Med Chem*. 2015;58(11):4550–4572.
43 Ding G, Liu HD, Huang Q, et al. HDAC6 promotes hepatocellular carcinoma progression by inhibiting P53 transcriptional activity. *FEBS Lett*. 2013;587(7):880–886.
44 Bae HJ, Jung KH, Eun JW, et al. MicroRNA-221 governs tumor suppressor HDAC6 to potentiate malignant progression of liver cancer. *J Hepatol*. 2015;63(2):408–419.
45 Tang C, Du Y, Liang Q, Cheng Z, Tian J. Development of a novel histone deacetylase-targeted near-infrared probe for hepatocellular carcinoma imaging and fluorescence image-guided surgery. *Mol Imaging Biol*. 2020;22(3):476–485.
46 Liu X, Xiang M, Tong Z, et al. Activatable fluorescence probe via self-immolative intramolecular cyclization for histone deacetylase imaging in live cells and tissues. *Anal Chem*. 2018;90(9):5534–5539.
47 Kim IS, Kim HS, Kim M, et al. Synthesis and evaluation of 2-[(18)F] fluoroethyltriazolesuberohydroxamine acid for histone deacetylase in a tumor model as a positron emission tomography radiotracer. *Cancer Biother Radiopharm*. 2018;33(2):52–59.
48 Meng Q, Liu Z, Li F, et al. An HDAC-targeted imaging probe LBH589-cy5.5 for tumor detection and therapy evaluation. *Mol Pharm*. 2015;12(7):2469–2476.
49 Wang F, Qu L, Ren F, et al. High-precision tumor resection down to few-cell level guided by NIR-IIb molecular fluorescence imaging. *Proc Natl Acad Sci U S A*. 2022;119(15):e2123111119.
50 Li C, Mi J, Wang Y, et al. New and effective EGFR-targeted fluorescence imaging technology for intraoperative rapid determination of lung cancer in freshly isolated tissue. *Eur J Nucl Med Mol Imaging*. 2022;50:494.
51 Duvic M, Vu J. Vorinostat: a new oral histone deacetylase inhibitor approved for cutaneous T-cell lymphoma. *Expert Opin Investig Drugs*. 2007;16(7):1111–1120.
52 Tang C, Du Y, Liang Q, Cheng Z, Tian J. *A selenium-containing selective histone deacetylase 6 inhibitor for targeted in vivo breast tumor imaging and therapy*. 2019.
53 Frangioni JV. In vivo near-infrared fluorescence imaging. *Curr Opin Chem Biol*. 2003;7(5):626–634.
54 Lee YS, Lim KH, Guo X, et al. The cytoplasmic deacetylase HDAC6 is required for efficient oncogenic tumorigenesis. *Cancer Res*. 2008;68(18):7561–7569.
55 Shan B, Yao TP, Nguyen HT, et al. Requirement of HDAC6 for transforming growth factor-beta1-induced epithelial-mesenchymal transition. *J Biol Chem*. 2008;283(30):21065–21073.
56 Jung KH, Noh JH, Kim JK, et al. Histone deacetylase 6 functions as a tumor suppressor by activating c-Jun NH2-terminal kinase-mediated beclin 1-dependent autophagic cell death in liver cancer. *Hepatology*. 2012;56(2):644–657.
57 Ryan QC, Headlee D, Acharya M, et al. Phase I and pharmacokinetic study of MS-275, a histone deacetylase inhibitor, in patients with advanced and refractory solid tumors or lymphoma. *J Clin Oncol*. 2005;23(17):3912–3922.
58 Kelly WK, O'Connor OA, Krug LM, et al. Phase I study of an oral histone deacetylase inhibitor, suberoylanilide hydroxamic acid, in patients with advanced cancer. *J Clin Oncol*. 2005;23(17):3923–3931.

59 Hendricks JA, Keliher EJ, Marinelli B, Reiner T, Mazitschek R. In vivo PET imaging of histone deacetylases by 18F- suberoylanilide hydroxamic acid (18F-SAHA). *J Med Chem*. 2011;54(15):5576–5582.
60 Boogerd LSF, Hoogstins CES, Schaap DP, et al. Safety and effectiveness of SGM-101, a fluorescent antibody targeting carcinoembryonic antigen, for intraoperative detection of colorectal cancer: a dose-escalation pilot study. *Lancet Gastroenterol Hepatol*. 2018;3(3):181–191.
61 de Gooyer JM, Elekonawo FMK, Bremers AJA, et al. Multimodal CEA-targeted fluorescence and radioguided cytoreductive surgery for peritoneal metastases of colorectal origin. *Nat Commun*. 2022;13(1):2621.
62 Lamberts LE, Koch M, de Jong JS, et al. Tumor-specific uptake of fluorescent bevacizumab-IRDye800CW microdosing in patients with primary breast cancer: a phase I feasibility study. *Clin Cancer Res*. 2017;23(11):2730–2741.